PAPER

Check for updates

Tunable orange-deep red photoluminescence in amorphous KZn$_{1-x}$Mn$_x$(PO$_3$)$_3$ phosphors and anti-counterfeiting applications†

Jiayue Jiang, [ID] [a,c] Hao Wang, [b] Tingting Zhao, [b] Yixuan Xu, [a] Junlong Li, [a,b,c] Hu Cheng, [ID] [a] Fei Zhang, [a] Dongliang Yang, [a] Yu Gong, [a] Chuanlong Lin, *[b] Xiaodong Li [ID] *[a] and Yanchun Li*[a]

Amorphous luminescence is a fascinating light emission phenomenon with significant implications for displays, sensors, and the anti-counterfeiting field. However, the development of amorphous materials is relatively limited due to the challenges in their synthesis and characterization, usually lagging behind those of their crystalline counterparts. This paper reports a triphosphate KZn$_{1-x}$Mn$_x$(PO$_3$)$_3$ ($0 \leq x \leq 1$) phosphor that can form two crystal phases (α-phase and β-phase) and an amorphous phase (Am-phase) by adjusting the synthesis temperature. Research shows that the Am-KZn$_{1-x}$Mn$_x$(PO$_3$)$_3$ phosphor exhibits superior luminescence properties compared to its crystalline counterparts. By varying the ratio of Zn/Mn, this amorphous phosphor can achieve multi-color photoluminescence (PL) ranging from orange to deep red (604 nm–693 nm), with a full width at half maximum (FWHM) of ~100 nm. In addition, the Am-KZn$_{1-x}$Mn$_x$(PO$_3$)$_3$ phosphor demonstrates fewer trap energy levels, while crystalline phosphors have abundant thermoluminescence (TL) traps. These structural and optical characteristics elucidate the luminescence mechanism of the phosphors dependent on Mn^{2+} and defects. Finally, by combining the PL and TL characteristics of the KZn$_{1-x}$Mn$_x$(PO$_3$)$_3$ phosphor with different phases and Mn concentrations, an anti-counterfeiting code method was designed, indicating that this material has great potential for applications in the field of anti-counterfeiting and information storage.

1. Introduction

Amorphous luminescent materials (*i.e.*, amorphous phosphors) have attracted increasing attention from researchers due to their outstanding luminescence properties, particularly their high luminescence efficiency, tunable emission wavelengths, and stable luminescence characteristics.[1–3] Since the discovery of amorphous glass luminescent materials, various types of amorphous phosphors, including perovskite-type,[4,5] silicon-based,[6–8] and metal–organic complexes,[9,10] have been extensively studied. For example, Zhou *et al.* found that the photoluminescence (PL) intensity of amorphous Ga$_2$O$_3$ nanofibers annealed at 873 K was two orders of magnitude higher

than that of β-Ga$_2$O$_3$ annealed at 973 K.[1] Sun reported that the transition of NaAlSiO$_4$:Eu^{2+} from an amorphous glass to a crystalline nepheline phase after annealing at different crystallization times can enable tunable color emissions ranging from blue to yellow.[11] Chen *et al.* reported that CsPbX$_3$ quantum dots protected by amorphous glass demonstrated remarkable heat and moisture resistance, retaining over 90% of their initial PL intensity even after 50 days.[12] These exceptional luminescence properties make amorphous materials promising for various application prospects in fields such as lighting, imaging, and information encryption.[13,14] However, research on these amorphous luminescent materials has been relatively limited due to the challenges in their preparation and characterization. Current studies on amorphous luminescent materials mostly focus on organic luminescent groups.[13,15] Nevertheless, amorphous inorganic luminescent materials demonstrate superior performance in terms of luminescence efficiency, stability, and the emission wavelength range. Therefore, in-depth research on such materials has important scientific value and application prospects.

For inorganic luminescent materials, rare-earth ions or transition metal ions are important activators in the host

aMulti-disciplinary Research Division of Institute of High Energy Physics, Chinese Academy of Sciences, Beijing 100049, P.R. China. E-mail: liyc@ihep.ac.cn, lixd@ihep.ac.cn

bCenter for High Pressure Science and Technology Advanced Research (HPSTAR), Beijing 100193, P.R. China. E-mail: chuanlong.lin@hpstar.ac.cn

cUniversity of Chinese Academy of Sciences, Beijing 100049, P.R. China

†Electronic supplementary information (ESI) available. See DOI: https://doi.org/10.1039/d5dt00007f

material, serving as luminescent centers. These ions can introduce defects and disrupt the periodic potential field of the ideal lattice, perturbing the local potential energy in the bandgap and forming trap levels that can capture charge carriers.[16] Currently, rare-earth ions such as Ce^{3+}, Eu^{2+}, and Pr^{3+} are commonly used as doping ions in most inorganic phosphors. However, rare-earth ions are expensive and resources are relatively scarce. In comparison, the transition metal ion manganese (Mn) is more economical and has better chemical stability.[17] In addition, the outer electron configuration of Mn ions is $3d^5$, which is directly exposed to the external environment, making it susceptible to the surrounding local coordination crystal fields, thereby improving the photoluminescence efficiency and broadening the emission range.[18–20] For example, ZnS:Mn exhibits excellent luminescence properties, with its photoluminescence (PL) spectrum showing a red shift under pressure, and mechanoluminescence (ML) exhibits strong luminescence under GPa-level pressures.[21,22] In addition, within the pressure range of 0–5.7 GPa, the PL intensity of Mn^{2+} and Eu^{3+} co-doped ZnS increases with rising pressure.[23] Therefore, compared to the f–f narrowband transitions of rare earth ions, the d–d broad-band transition of Mn ions can lead to a greater range of potential applications.

In recent years, phosphate phosphors have been proved to have suitable bandgaps for the manufacturing of white LEDs and sensors, and they are considered more environmentally friendly compared to traditional phosphors.[24–26] However, most of these phosphors exist in the form of crystalline compounds, which limits the regulation of their luminescence properties. Compared to crystalline phosphors, amorphous phosphors lack long-range order and only exhibit short-range atomic order, providing significant advantages in luminescence performance. This makes amorphous phosphors enormously promising for future new luminescent materials. To improve the performance of phosphate phosphors, preparing their amorphous structures is an effective strategy. For instance, Jiang *et al.* prepared Eu^{3+}-doped PBCFS amorphous glass, which exhibits tunable orange-red luminescence.[27] Notably, previous studies have shown that the triphosphate AB $(PO_3)_3$ (A = alkali, B = Mg/Zn) materials have excellent luminescence properties and thermal stability, indicating significant potential for application in the lighting field.[24–26] However, there are currently no reports on the amorphous luminescence properties of these materials.

Inspired by the above, we synthesize a series of $KZn_{1-x}Mn_x(PO_3)_3$ phosphors using a high-temperature solid-state reaction method and test their luminescence properties. Among these, the Am-$KZn_{1-x}Mn_x(PO_3)_3$ phosphor exhibits excellent luminescence properties, a broad emission spectrum, and a tunable luminescence wavelength by adjusting the Mn concentration. Additionally, the Am-$KZn_{1-x}Mn_x(PO_3)_3$ phosphor demonstrates fewer trap energy levels, while the β-$KZn_{1-x}Mn_x(PO_3)_3$ phosphor exhibits better thermoluminescence (TL) behavior. Based on the PL and TL characteristics, we design an anti-counterfeiting model for information

encryption and retrieval. In summary, this work not only discovers an amorphous $KZn_{1-x}Mn_x(PO_3)_3$ phosphor with outstanding optical properties, but also reveals the potential application of the $KZn_{1-x}Mn_x(PO_3)_3$ phosphor in the anti-counterfeiting field.

2. Experimental

2.1 Synthesis of materials

A series of $KZn_{1-x}Mn_x(PO_3)_3$ ($0 \leq x \leq 1$) phosphors were synthesized *via* a high-temperature solid-state reaction method. The mixed analytical reagents $K_2CO_3 \cdot 1/2H_2O$, ZnO, MnO_2, and $NH_4H_2PO_4$ were used as the raw materials according to the stoichiometric composition and thoroughly ground in an agate mortar with absolute ethanol. The homogeneous mixtures were transferred into alumina crucibles and heated at different temperatures for 20 hours under an ambient atmosphere. After cooling the resultant products to room temperature, they were ground into powders again for further characterization.

2.2 Characterization and luminescence testing

The room-temperature X-ray diffraction (XRD) patterns of the synthesized phosphors were collected using a Bruker-D8 X-ray diffractometer. The morphology and the energy distribution of the samples were characterized using scanning electron microscopy (SEM, JEOL, Japan) and energy dispersive spectrum (EDS). The valence state of Mn in the samples was analyzed through X-ray absorption near edge structure (XANES) at the 4B9B beamline, Beijing Synchrotron Radiation Facility (BSRF). The high-temperature XRD patterns were measured at the 1 W1A beamline, BSRF. The photoluminescence (PL) spectra and decay curves were recorded using a steady-state transient fluorescence spectroscopy system (Ideaoptics, Beijing, China). The PLE spectra were collected using a personalized steady-state transient fluorescence spectrometer (FS5, Edinburgh, England). The thermoluminescence (TL) spectra and afterglow lifetime curves were collected with a multifunctional defect fluorescence spectrometer (LTTL-3DS, Aison, China) after being irradiated at 254 nm UV light for 2 minutes.

2.3 Preparation of mixed film

The $KZn_{1-x}Mn_x(PO_3)_3$ powder was mixed with polydimethylsiloxane (PDMS, SYLGARD 184, Dow Corning) and a curing agent in a weight ratio of $10:10:1$. The mixture was then stirred in a beaker for 5 minutes to obtain a well-mixed colloidal solution, which was subsequently poured into a mold and annealed in an oven at 333 K for 2 hours to form a film.

3. Results and discussion

3.1 Characterization of $KZn_{1-x}Mn_x(PO_3)_3$ phosphor

Previous studies have shown that the $KZn(PO_3)_3$ crystal can serve as an effective host for Mn-activated luminescent ions.[24]

Due to the same valence state and similar ion radius of Mn^{2+} compared to Zn^{2+} (the ionic radii of Zn^{2+} and Mn^{2+} are 0.74 Å and 0.83 Å, respectively),[24] it is believed that Mn^{2+} ions are more likely to replace Zn^{2+} ions, allowing the $KZn_{1-x}Mn_x(PO_3)_3$ crystal to become a phosphor. Through the high-temperature solid-state reaction method, we find that $KZn_{1-x}Mn_x(PO_3)_3$ ($0 \leq x \leq 1$) phosphors can form different phases at various sintering temperatures. X-ray powder diffraction analysis is used to study the crystal structures of the three phases. In addition to the previously reported α-phase (trigonal structure, $R32$ space group) and β-phase (hexagonal structure, $P\bar{6}c2$ space group),[24] a structure with an amorphous nature is also obtained (Fig. 1a, all XRD patterns are shown in Fig. S1†). Notably, the slightly larger ionic radius of Mn^{2+} compared to Zn^{2+} results in the diffraction peaks of the three phases shifting to lower angles as the concentration of Mn increases (Fig. 1b), which indicates the expansion of the lattice cell. In addition, at any Zn/Mn ratio, the diffraction peaks of the $KZn_{1-x}Mn_x(PO_3)_3$ phosphors did not exhibit the impurity peaks of the raw materials, suggesting that the synthesis of all raw materials is complete.

Generally, phase diagrams provide a concise method for observing phase distribution, and thus the $KZn_{1-x}Mn_x(PO_3)_3$ phase diagram (Fig. 1c) clearly reveals the synthesis conditions for the α-phase, β-phase, and Am-phase through targeted modulation of Mn concentration and synthesis temperature. It can be seen that the thermal region of the α-phase is relatively narrow, while the areas for the β-phase and Am-phase are more extensive. The α-phase begins to appear at very low Mn concentrations when the synthesis temperature is below 773 K. As the synthesis temperature decreases, the Mn concentration gradually increases, reaching $x = 0.2$ for the α-phase at 673 K. It can be inferred that at lower synthesis temperatures, the α-phase can be synthesized with higher Mn concentrations. In

contrast, the Am-phase can only be synthesized at higher temperatures (around 943 K), and the Mn concentration of the Am-phase increases with the synthesis temperature. At 1173 K, Mn can completely replace Zn in the Am-phase. Under other conditions, the synthesized phase is the β-phase and there is a narrow coexistence zone between the α-phase and β-phase when the synthesis temperature is below 773 K. We speculate that the variation in phases of $KZn_{1-x}Mn_x(PO_3)_3$ phosphors at different synthesis temperatures and Mn concentrations may be related to the equilibrium activation barrier. At 673 K and low Mn concentrations, the system can form the α-phase but lacks sufficient thermal energy to overcome the activation barrier for forming the β-phase. At the high temperature of 1173 K, the increased thermal energy of atoms and molecules makes them more likely to overcome the energy barriers and form an amorphous structure. However, at a synthesis temperature of 673 K, introducing more Mn ($x > 0.2$) can reduce the activation barrier of the β-phase, thereby promoting the generation of the β-$KZn_{1-x}Mn_x(PO_3)_3$ phosphor at lower synthesis temperatures.

Fig. 1d shows the scanning electron microscopy (SEM) images and elemental mapping of the Am-$KZn_{0.8}Mn_{0.2}(PO_3)_3$ phosphor. Compared to the morphology of the α-$KZn_{0.8}Mn_{0.2}(PO_3)_3$ phosphor and the β-$KZn_{0.8}Mn_{0.2}(PO_3)_3$ phosphor (Fig. S2†), the surface of the Am-$KZn_{0.8}Mn_{0.2}(PO_3)_3$ phosphor appears smoother and more uniform. In addition, elemental mapping analysis reveals the homogeneous distribution of K, Zn, P, O, and Mn in samples. To investigate the changes in the valence state of Mn during the synthesis process, X-ray absorption near edge structure (XANES) is used to characterize the valence of Mn ions. As shown in Fig. 1e, the positions of the main peak in the Mn L-edge XANES spectra of α-$KZn_{0.9}Mn_{0.1}(PO_3)_3$, β-$KZn_{0.9}Mn_{0.1}(PO_3)_3$, and Am-$KZn_{0.9}Mn_{0.1}(PO_3)_3$ phosphors are observed at about 640.3 eV, which corresponds to the previously reported position of divalent Mn.[28,29] This indicates that self-reduction from Mn^{4+} to Mn^{2+} occurred during the synthesis process and confirms the successful incorporation of Mn ions into the samples. The self-reduction of Mn is crucial for the formation of defects and the induction of luminescence.

3.2 Photoluminescence (PL) properties and mechanisms of $KZn_{1-x}Mn_x(PO_3)_3$ phosphor

To further explore the difference between the crystalline $KZn_{1-x}Mn_x(PO_3)_3$ phosphor and the amorphous $KZn_{1-x}Mn_x(PO_3)_3$ phosphor, we present the luminescence characteristics of $KZn_{0.8}Mn_{0.2}(PO_3)_3$ monomers with different structures as shown in Fig. 2a. The photoluminescence (PL) spectra indicate that $KZn_{0.8}Mn_{0.2}(PO_3)_3$ phosphors with different phases exhibit a tunable color ranging from orange to red. Notably, the crystalline $KZn_{0.8}Mn_{0.2}(PO_3)_3$ phosphor exhibits blue emission characteristics of the matrix, which may be attributed to intrinsic defects formed during the synthesis process. The photoluminescence excitation (PLE) spectra show a series of excitation peaks within the range of 300–500 nm, attributed to the distinct d–d electron transitions
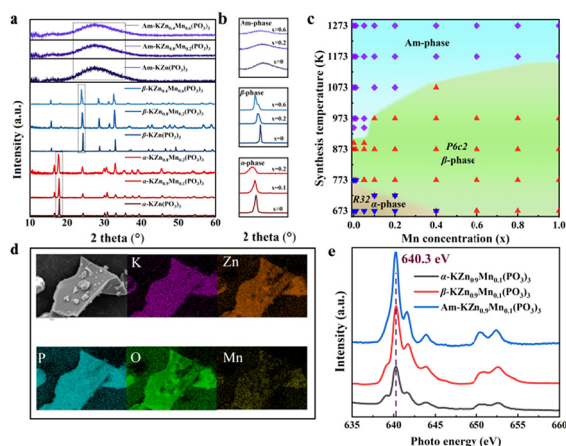

Fig. 1 Characterization of $KZn_{1-x}Mn_x(PO_3)_3$ phosphors with different phases. (a) The selected XRD patterns of $KZn_{1-x}Mn_x(PO_3)_3$ phosphors at different synthesis temperatures. (b) The enlarged view of the partial XRD patterns of $KZn_{1-x}Mn_x(PO_3)_3$ phosphors with different phases; x represents the proportion of Mn in Zn/Mn. (c) The phase diagram of $KZn_{1-x}Mn_x(PO_3)_3$ phosphors at different synthesis temperatures. (d) SEM images and elemental mapping of Am-$KZn_{0.8}Mn_{0.2}(PO_3)_3$ phosphors. (e) XANES of the Mn L-edge for three phases.
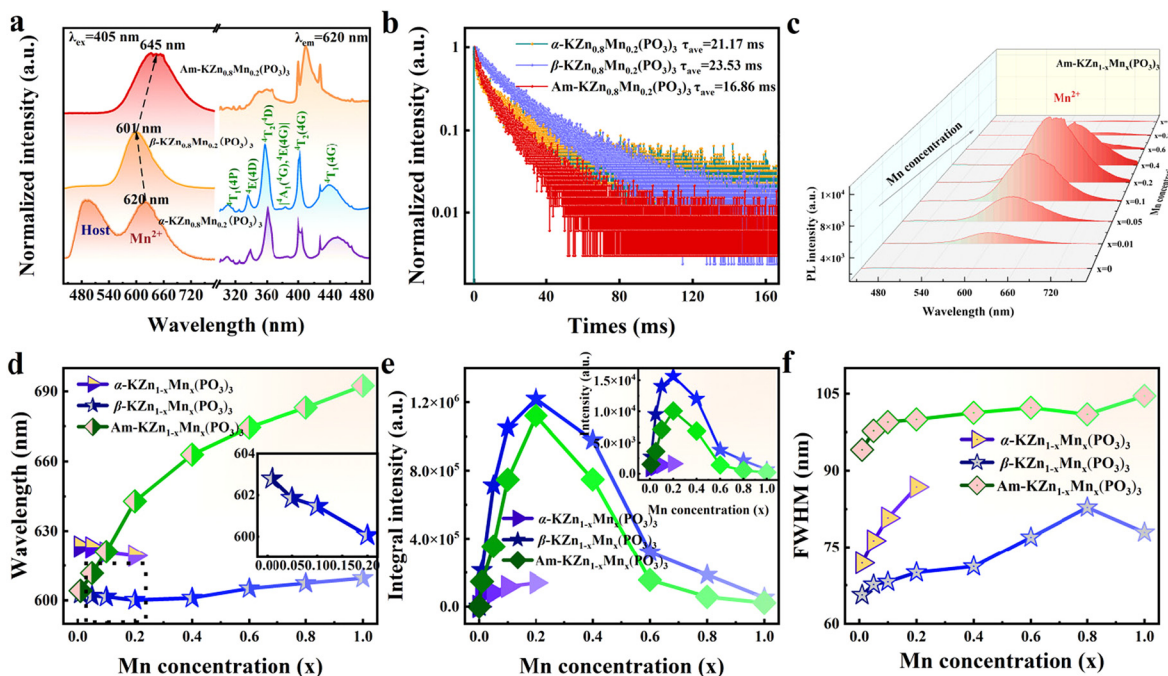
Fig. 2 Phosphorescence properties of $KZn_{1-x}Mn_x(PO_3)_3$ phosphors with different phases. (a) The PL and PLE spectra of $KZn_{0.8}Mn_{0.2}(PO_3)_3$ phosphors for different phases. (b) The decay curves of $KZn_{0.8}Mn_{0.2}(PO_3)_3$ phosphors for different phases. (c) The 3D PL spectra of $Am-KZn_{1-x}Mn_x(PO_3)_3$ phosphors. (d) Peak positions of PL spectra for $KZn_{1-x}Mn_x(PO_3)_3$ phosphors at different phases and Mn concentrations. The inset is the wavelength blue shift of the $\beta-KZn_{1-x}Mn_x(PO_3)_3$ phosphor with the Mn concentration ranging from 0.01 to 0.2. (e) The PL integrated intensities of $KZn_{1-x}Mn_x(PO_3)_3$ phosphors at different phases and Mn concentrations. The illustration is the value at the strongest point of the PL peak. (f) The FWHM of $KZn_{1-x}Mn_x(PO_3)_3$ phosphors with different phases and Mn concentrations.

of Mn^{2+} ions.[24–26,30] Generally, the manipulation of the spectral characteristics is linked to changes in the coordination environment of Mn^{2+}. Therefore, the disordered structure of the amorphous state will result in differences in the PLE spectra compared to crystalline structures.

To further investigate the active centers, the PL decay curves of the $KZn_{0.8}Mn_{0.2}(PO_3)_3$ phosphor with different phases are collected at 405 nm excitation. Interestingly, the $KZn_{1-x}Mn_x(PO_3)_3$ phosphor has only one type of Mn^{2+} emitter, but the PL decay does not follow a monoexponential decay function. Instead, it can be fitted with a biexponential function ($I = A_1 \exp(-t/\tau_1) + A_2 \exp(-t/\tau_2)$, as shown in Fig. 2b; the fitting results of lifetime components and relative amplitudes are shown in Table S1†). This deviation from the monoexponential decay mechanism may be attributed to the influence of traps and Mn concentrations (see Fig. S3 and Table S2† for PL decay curves at low Mn concentrations).[31] It is worth noting that due to the complex internal decay mechanism of the amorphous phosphor, a biexponential decay model is used to fit the PL decay for both low and high Mn concentrations to provide a simple and effective description of the lifetime. In addition, the lifetime of the amorphous phosphor is shorter than that of the crystalline phosphor, which may result from a wider distribution of emission centers or the presence of multiple recombination mechanisms in the amorphous state.

The 3D PL spectra of $Am-KZn_{1-x}Mn_x(PO_3)_3$ phosphors are shown in Fig. 2c (the PL spectra of the crystalline phosphors

are shown in Fig. S4†). For a more detailed analysis of the effects of different phases and Mn concentrations on the luminescence properties, the original PL spectra are extracted. Fig. 2d shows the central positions of peaks in the PL spectra of the $KZn_{1-x}Mn_x(PO_3)_3$ phosphor with different phases and Mn concentrations. The results indicate that as the Mn concentration increases from 0.01 to 0.2, the peak wavelength of the α-phase shifts from 619 nm to 624 nm. Similarly, the peak wavelength of the β-phase shifts from 603 nm to 600 nm with the same increase in Mn concentration. This blue shift can be explained by the reduction in the degree of energy level splitting resulting from a weaker crystal field strength.[32] In contrast, as the Mn concentration further increases from 0.2 to 1, the red shift in the central wavelength (from 600 nm to 610 nm) may be due to the formation of Mn^{2+} pairs, leading to a reduction in the energy gap between the $^4T_1$ and $^6A_1$.[33] For the Am-phase, the wavelength of the luminescent center increases from 604 to 693 nm as the Mn concentration increases from 0.01 to 1, almost covering the emission ranges of both the α-phase and β-phase. While the peak wavelengths of α-phase and β-phase show slight changes with the variation of Mn concentration, the wavelength of the PL peak in the Am-phase exhibits a significant red shift as the Mn concentration increases. This discrepancy may stem from the relatively fixed interactions between the site of Mn substituting for Zn and surrounding atoms in the crystalline phase, which limits the impact on the crystal field, leading to limited changes in the

emission wavelength. In contrast, the amorphous material lacks long-range order, and variations in Mn concentration change the surrounding coordination environment (such as the inter-ion distance, coordination number, or local symmetry), allowing Mn to be embedded in various ways, resulting in more flexible changes in the emission wavelength.

Fig. 2e shows a comparison of the PL-integrated intensities of Mn^{2+} luminescent centers in the $KZn_{1-x}Mn_x(PO_3)_3$ phosphor with different phases and Mn concentrations. The result indicates that at the same Mn concentration, the integrated intensities of the $Am-KZn_{1-x}Mn_x(PO_3)_3$ phosphor and the $\beta-KZn_{1-x}Mn_x(PO_3)_3$ phosphor are similar, and both are one order of magnitude higher than that of the $\alpha-KZn_{1-x}Mn_x(PO_3)_3$ phosphor. Additionally, the emission intensities of $KZn_{1-x}Mn_x(PO_3)_3$ phosphors with all three phases gradually increase with a rising Mn concentration, reaching a maximum at $x = 0.2$, after which the emission intensities of $\beta-KZn_{1-x}Mn_x(PO_3)_3$ and $Am-KZn_{1-x}Mn_x(PO_3)_3$ phosphors decrease at $x > 0.2$. The increase in emission intensity before $x = 0.2$ is attributed to an increase in the number of luminescent centers with an increasing activator concentration. However, beyond $x = 0.2$, the concentration quenching effect is enhanced, and the non-radiative energy transfer of Mn^{2+} ions in the host lattice increases, causing a decrease in emission intensity.[34] The inset of Fig. 2e shows the strongest value of the PL peak, indicating that the emission intensity of the $\beta-KZn_{1-x}Mn_x(PO_3)_3$ phosphor is about 1.4 times that of the $Am-KZn_{1-x}Mn_x(PO_3)_3$ phosphor, while the emission intensity of the $Am-KZn_{1-x}Mn_x(PO_3)_3$ phosphor is about 4 times higher than that of the $\alpha-KZn_{1-x}Mn_x(PO_3)_3$ phosphor at the same Mn concentration. Fig. 2f compares the full width at half maximum (FWHM) of the $KZn_{1-x}Mn_x(PO_3)_3$ phosphor with different phases and Mn concentrations. The result indicates that the FWHM of the $KZn_{1-x}Mn_x(PO_3)_3$ phosphor with three phases generally shows an increasing trend with an increasing Mn concentration. At the same Mn concentration, the $\beta-KZn_{1-x}Mn_x(PO_3)_3$ phosphor demonstrates the narrowest FWHM, while the $Am-KZn_{1-x}Mn_x(PO_3)_3$ phosphor exhibits the widest FWHM (about 100 nm). The broad FWHM of the $Am-KZn_{1-x}Mn_x(PO_3)_3$ phosphor may be related to the presence of more localized electronic states caused by the structural disorder. The existence of localized electronic states contributes to the complexity of the energy level structure in the material, leading to multiple emission channels during the luminescence process, thereby increasing the spectral FWHM.[35] These results show the commendable performance of the $Am-KZn_{1-x}Mn_x(PO_3)_3$ phosphor in PL, making it suitable for diverse applications, such as applications in lighting and display technologies.

3.3 Thermoluminescence (TL) and afterglow (AG) properties of the $KZn_{1-x}Mn_x(PO_3)_3$ phosphor

The TL analysis is employed to monitor the detrapping behavior of charge carriers in defect centers, laying the foundation for long-afterglow (LAG) studies.[36] The TL curve of the $KZn_{1-x}Mn_x(PO_3)_3$ phosphor is collected at a heating rate of 1 K s^{-1} after exposure to 254 nm UV light for 2 minutes. Fig. S5†

shows TL curves of all samples, and it was found that the Mn concentration with the strongest TL emission is lower than the Mn concentration with the strongest PL emission. The strongest luminescence phenomenon of PL and TL at different Mn concentrations is closely related to energy transfer. Due to the involvement of traps, energy transfer can occur between adjacent luminescent activators over longer ionic distances, resulting in a decrease in the quenching concentration of TL.[37] In addition, the Gaussian decomposition method fitting the TL curve of the $\alpha-KZn_{0.99}Mn_{0.01}(PO_3)_3$ phosphor shows that at least two TL peaks are located at 429.7 K and 501.3 K (Fig. 3a). The TL curve of the $\beta-KZn_{0.95}Mn_{0.05}(PO_3)_3$ phosphor is decomposed into at least three curves, with peak centers located at 346.2 K, 450.2 K, and 520.5 K (Fig. 3b). This indicates that the two crystal phases have different TL characteristics. Notably, the $Am-KZn_{1-x}Mn_x(PO_3)_3$ phosphor exhibits almost no TL signals, which may be attributed to their disordered structure resulting in fewer fixed defects (Fig. 3c and Fig. S5†).

Fig. 3d compares the PL and TL spectra of the $\beta-KZn_{0.95}Mn_{0.05}(PO_3)_3$ phosphor. The TL emission spectrum signal is detected at a temperature of 449 K. The wavelength of the TL emission spectrum (with the highest emission intensity at 595.93 nm and FWHM at 75.59 nm) is similar to that of the PL emission spectrum (with the highest emission intensity at 601.33 nm and FWHM at 67.25 nm), indicating that TL emission is also caused by the Mn^{2+} emitter. The slight blue shift and larger FWHM of the TL spectrum may be due to the influence of temperature. In addition, temperature-dependent XRD analysis shows that the structures of the α-phase, β-phase, and Am-phase remain stable from room temperature to 673 K (Fig. S6†), indicating that no phase transition occurs during the measurement of the TL curve.

The trap depth can be calculated by the Randall and Wilkins' method,[38] and the trap depth of most room-temperature long-afterglow materials ranges from 0.5 eV to 0.75 eV. Electrons captured in the shallow trap can be easily released by the thermal vibrations of the lattice, leading to the formation of long afterglow luminescence.[39,40] Fig. 3e shows the fitting curve of the $\beta-KZn_{0.95}Mn_{0.05}(PO_3)_3$ phosphor with time constants of 2.06 s and 56.48 s, and the average afterglow lifetime is 56.47 s, indicating that the material belongs to the category of long-afterglow materials. Fig. 3f compares the average afterglow lifetime of the $KZn_{1-x}Mn_x(PO_3)_3$ phosphor with different phases and Mn concentrations. The result indicates that both the $\alpha-KZn_{1-x}Mn_x(PO_3)_3$ phosphor and the $Am-KZn_{1-x}Mn_x(PO_3)_3$ phosphor exhibit very short average afterglow lifetimes, while the $\beta-KZn_{1-x}Mn_x(PO_3)_3$ phosphor exhibits a longer average afterglow lifetime. As the Mn concentration increases, the average afterglow lifetimes of the $\beta-KZn_{1-x}Mn_x(PO_3)_3$ phosphor initially increase and then decrease, with the $\beta-KZn_{0.95}Mn_{0.05}(PO_3)_3$ phosphor having the longest lifetimes. The inset shows the shallow trap density of the $KZn_{1-x}Mn_x(PO_3)_3$ phosphor. It is found that the changing trend of shallow trap density as the Mn concentration increases is nearly consistent with the changing trend of afterglow lifetime, which indicates a close relationship between the room temperature afterglow lifetime and shallow
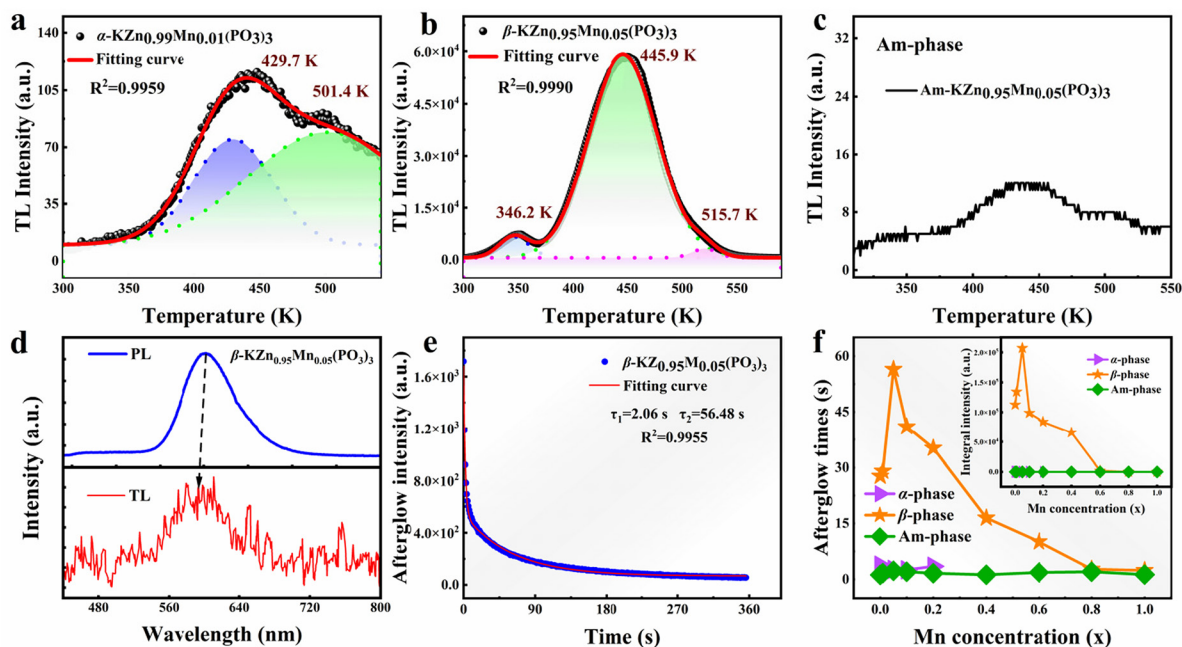
Fig. 3 Defect research of $KZn_{1-x}Mn_x(PO_3)_3$ phosphors with different phases. The TL fitting curves of (a) the α-$KZn_{0.99}Mn_{0.01}(PO_3)_3$ phosphor and (b) the β-$KZn_{0.95}Mn_{0.05}(PO_3)_3$ phosphor at heating rates of 1 K s^{-1}. (c) The TL curve of the Am-$KZn_{1-x}Mn_x(PO_3)_3$ phosphor at heating rates of 1 K s^{-1}. (d) Comparison of the PL and TL spectra of the β-$KZn_{0.95}Mn_{0.05}(PO_3)_3$ phosphor. (e) The fitted afterglow curve of the β-$KZn_{0.95}Mn_{0.05}(PO_3)_3$ phosphor after exposure to 254 nm UV light for 2 minutes. (f) The comparison of the afterglow lifetime of the $KZn_{1-x}Mn_x(PO_3)_3$ phosphor at different phases and Mn concentrations. The inset is the comparison of shallow trap density in different phases and Mn concentrations.

traps. The long afterglow property of the β-$KZn_{1-x}Mn_x(PO_3)_3$ phosphor makes it suitable for emergency lighting and self-luminous labeling.

3.4 The mechanism of luminescence in the $KZn_{1-x}Mn_x(PO_3)_3$ phosphor

Based on the above experiments and analyses, Fig. 4 provides a schematic diagram of the luminescence mechanism. When excited by UV light, electrons located in the valence band (VB) will be pumped to the conduction band (CB, process 1). Some of the electrons and holes will be captured by defects, while others will undergo non-radiative recombination. For the PL process, the blue emission of the host material is mainly dominated by electrons captured by intrinsic defects generated during the sintering process (process 2), while the luminescence of Mn^{2+} results from energy transfer through non-radiative recombination of electrons and holes (process 3). For the TL process, charge carriers captured will be de-trapped during heat treatment (process 4), then released into the excited state and returned to the ground state to combine with holes, resulting in luminescence (process 5). The luminescence mechanism of the β-$KZn_{1-x}Mn_x(PO_3)_3$ phosphor is similar to that of the α-$KZn_{1-x}Mn_x(PO_3)_3$ phosphor. However, electrons at shallow trap levels can transition to the luminescence center under room-temperature thermal vibration or tunneling effects, leading to long afterglow luminescence in the material (Fig. 4b). In addition, the luminescence process of the Am-$KZn_{1-x}Mn_x(PO_3)_3$ phosphor does not involve the TL process

(Fig. 4c). To analyze the formation of defects for capturing electrons, Fig. 4d and e show the crystal structure and defect formation process. During this process, electrons and holes are captured by V''_{Zn}, O''_i, and $V_O^{\bullet\bullet}$ defects. V''_{Zn} defects mainly originate from the self-reduction of Mn^{4+} to Mn^{2+} within the host lattice, while O''_i and $V_O^{\bullet\bullet}$ defects are primarily caused by the atmospheric conditions during synthesis.[41] Fig. 4d depicts the process of defect formation and the reduction equation of Mn of the α-$KZn_{1-x}Mn_x(PO_3)_3$ phosphor. To maintain charge neutrality, a single Mn^{4+} may occupy two Zn^{2+} lattice sites, leading to the formation of a Zn vacancy with two negative charges (V''_{Zn}) and Mn sites with two positive charges ($Mn_{Zn}^{\bullet\bullet}$). During the high-temperature synthesis process, the two electrons of V''_{Zn} will transfer to $Mn_{Zn}^{\bullet\bullet}$, thus the Mn^{4+} reduces to Mn^{2+}.[34] In contrast to the α-$KZn_{1-x}Mn_x(PO_3)_3$ phosphor, due to its unique structure, the β-$KZn_{1-x}Mn_x(PO_3)_3$ phosphor will introduce interstitial oxygen defects (O''_i) when synthesized in an oxygen-rich environment. The Mn^{4+} occupies Zn^{2+} sites will form $Mn_{Zn}^{\bullet\bullet}$, and O''_i with two negative charges will act as a donor, transferring two electrons to $Mn_{Zn}^{\bullet\bullet}$, thereby reducing Mn^{4+} to Mn^{2+} (Fig. 4e).[30] However, the TL test indicates that the Am-$KZn_{1-x}Mn_x(PO_3)_3$ phosphor has almost no defects, and further research is needed on its self-reduction behavior.

3.5 Anti-counterfeiting application of $KZn_{1-x}Mn_x(PO_3)_3$ phosphor

Due to the multicolor manipulation properties of the Am-$KZn_{1-x}Mn_x(PO_3)_3$ phosphor at different Mn concentrations,
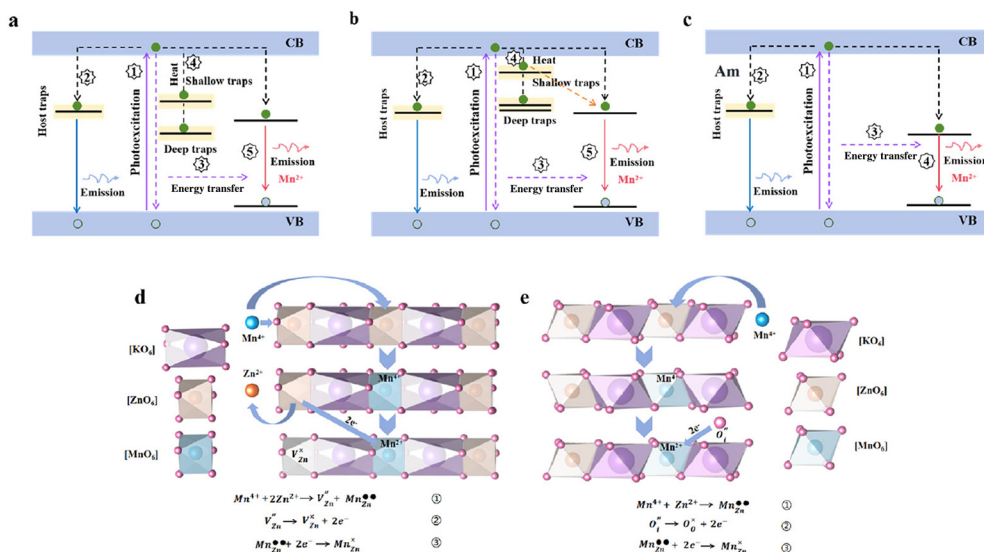
Fig. 4 Defect-assisted luminescence mechanism. The mechanism diagram of luminescence for (a) the α-KZn$_{1-x}$Mn$_x$(PO$_3$)$_3$ phosphor, (b) the β-KZn$_{1-x}$Mn$_x$(PO$_3$)$_3$ phosphor, and (c) the Am-KZn$_{1-x}$Mn$_x$(PO$_3$)$_3$ phosphor. Green solid circles = electrons; green hollow circles = holes; purple solid arrows = photoexcitation; vertical purple dashed arrows = recombination; horizontal purple dashed arrows = energy transfer; black dashed arrows = electron trapping or release; pink solid arrows = Mn^{2+} emission; blue solid arrows = host emission; and orange dashed arrows = tunneling effects. Sketch map of the crystal structure and defects and the corresponding defect reaction equations for (d) the α-KZn$_{1-x}$Mn$_x$(PO$_3$)$_3$ phosphor and (e) the β-KZn$_{1-x}$Mn$_x$(PO$_3$)$_3$ phosphor.

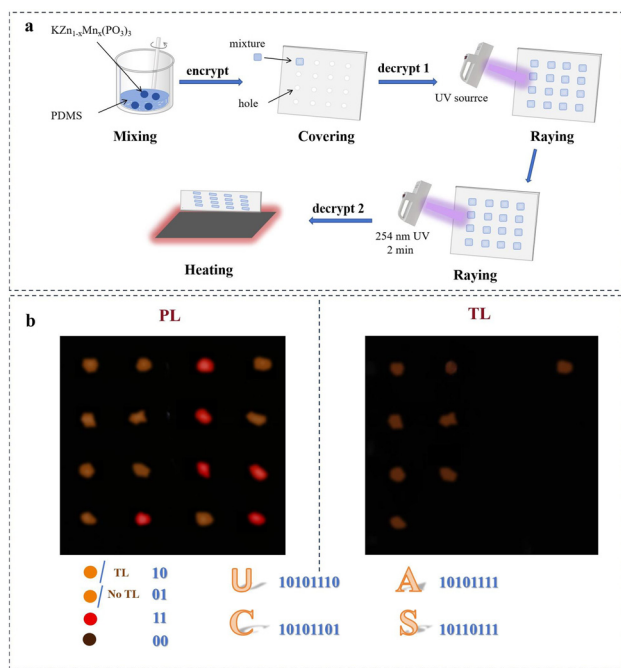**Fig. 5** Demonstration of the anti-counterfeiting application potential of KZn$_{1-x}$Mn$_x$(PO$_3$)$_3$ phosphor. (a) Schematic diagram for the application of KZn$_{1-x}$Mn$_x$(PO$_3$)$_3$ phosphor with different phases in anti-counterfeiting encryption. First, the phosphor is mixed with PDMS to obtain a uniform mixture. Next, the mixture is applied to perforated tin foil. Then, a UV light source is used to irradiate it, producing a set of luminescence effects (PL). Subsequently, it is exposed to 254 nm UV light for 2 minutes and then heated on a heating platform to obtain another set of luminescence effects (TL). (b) The decryption of the encoded information using UV light and heat.

combined with the Am-KZn$_{1-x}$Mn$_x$(PO$_3$)$_3$ phosphor lacking TL behavior and the β-KZn$_{1-x}$Mn$_x$(PO$_3$)$_3$ phosphor with strong TL behavior, we design a functional plate that requires double decryption to enhance anti-counterfeiting and information storage security. Fig. 5a shows a schematic diagram of the encryption–decryption process. KZn$_{1-x}$Mn$_x$(PO$_3$)$_3$ powders are mixed with PDMS to form information storage films and coated on a sample plate. The information is encrypted into the ASCII code through PL color (the luminescent sites are shown in the CIE diagram, as shown in Fig. S7†) and the presence or absence of TL, a single decryption method cannot obtain complete information. According to the PL colors and TL properties, the color codes for orange/with TL, orange/without TL, red, and non-emitting regions are encoded as 10, 01, 11, and 00, respectively. To demonstrate the anti-counterfeiting effect, the ASCII codes for the characters "U", "C", "A", and "S" are compiled (Fig. 5b). By analyzing the arrangement of different PL colors in each row and the existence status of TL, different characters can be decoded. This PL + TL dual decryption method increases the technical threshold and cost of counterfeiting compared to a single excitation step, while also achieving higher dimensional information output, thereby significantly enhancing anti-counterfeiting capabilities and improving the security of information storage.

4. Conclusion

In summary, this study presents three different phases (α-phase, β-phase, and Am-phase) of the KZn$_{1-x}$Mn$_x$(PO$_3$)$_3$ ($0 \leq x \leq 1$) phosphor by systematically varying the synthesis temp-

erature. Under 405 nm UV excitation, the Am-KZn$_{1-x}$Mn$_x$(PO$_3$)$_3$ phosphor exhibits a wide tunable spectral range, with the PL wavelength being tuned from 604 nm to 693 nm (from orange to deep red) by adjusting the Mn concentration. This color tunability may be related to the disorder in the Am-phase, allowing Mn to be incorporated into the lattice in multiple ways. Additionally, the PL integral intensities of the Am-phase and β-phase are similar, while the intensity of the Am-phase is about ten times greater than that of the α-phase. The TL results indicate that the Am-KZn$_{1-x}$Mn$_x$(PO$_3$)$_3$ phosphor displays a lower TL signal due to insufficient internal defects, while the TL excitation of the β-KZn$_{1-x}$Mn$_x$(PO$_3$)$_3$ phosphor is more efficient. Finally, we design a dual anti-counterfeiting encoding method based on the emission color tunability of the Am-phase and its distinct TL behavior compared to the β-phase. This method has the potential to enhance the security of information storage and demonstrates significant potential for applications in the anti-counterfeiting field.

Author contributions

Jiayue Jiang, Chuanlong Lin, and Yanchun Li conceived the investigation. Jiayue Jiang, Hao Wang, Tingting Zhao, Yixuan Xu, and Junlong Li performed the experiments. Jiayue Jiang, Hao Wang, Xiaodong Li, and Yanchun Li were involved in the analyses and interpretation of data. Jiayue Jiang wrote the manuscript with the help of Hu Cheng, Fei Zhang, Dongliang Yang, Yu Gong, Chuanlong Lin, Xiaodong Li, and Yanchun Li.

Data availability

The authors declare that the data supporting the findings of this study are available within the article and its ESI.† Extra data are available from the corresponding authors upon reasonable request.

Conflicts of interest

The authors declare no competing interests.

Acknowledgements

References

1 T. Zhou, P. Chen, S. Hu, Y. Yan, W. Pan and H. Li, *Ceram. Int.*, 2016, **42**, 6467–6474.

2 X. Di, L. Shen, J. Jiang, M. He, Y. Cheng, L. Zhou, X. Liang and W. Xiang, *J. Alloys Compd.*, 2017, **729**, 526–532.

3 S. Lin, H. Lin, C. Ma, Y. Cheng, S. Ye, F. Lin, R. Li, J. Xu and Y. Wang, *Light: Sci. Appl.*, 2020, **9**, 22.

4 P. S. Pizani, H. C. Basso, F. Lanciotti and T. M. Boschi, *Appl. Phys. Lett.*, 2002, **81**, 253–255.

5 S. Yoon, M. Seo, I. S. Kim, K. Lee and K. Woo, *Small*, 2023, **19**, e2206311.

6 L. Canham, *Faraday Discuss.*, 2020, **222**, 10.

7 P. Zhang, L. Zhang, Y. Wu, S. Wang and X. Ge, *Opt. Express*, 2018, **26**, 31617.

8 G. Vaccaro, S. Agnello, G. Buscarino, M. Cannas and L. Vaccaro, *J. Non-Cryst. Solids*, 2011, **357**, 1941–1944.

9 B. Zhou and D. Yan, *Adv. Funct. Mater.*, 2023, **33**, 2300735.

10 T. D. Bennett and A. K. Cheetham, Amorphous Metal–Organic Frameworks, *Acc. Chem. Res.*, 2014, **47**, 1555–1562.

11 Y. Sun, X. Zhou, Z. Lun, K. Han, P. Xiong and Z. Xia, *Adv. Funct. Mater.*, 2024, 2406336.

12 S. Chen, J. Lin, S. Zheng, Y. Zheng and D. Chen, *Adv. Funct. Mater.*, 2023, **33**, 2213442.

13 D. Guo, W. Wang, K. Zhang, J. Chen, Y. Wang, T. Wang, W. Hou, Z. Zhang, H. Huang, Z. Chi and Z. Yang, *Nat. Commun.*, 2024, **15**, 3598.

14 Y. J. Ma, G. Xiao, X. Fang, T. Chen and D. Yan, *Angew. Chem., Int. Ed.*, 2023, **62**, e202217054.

15 L. Gu, H. Wu, H. Ma, W. Ye, W. Jia, H. Wang, H. Chen, N. Zhang, D. Wang, C. Qian, Z. An, W. Huang and Y. Zhao, *Nat. Commun.*, 2020, **11**, 944.

16 P. Zhang, Y. Bai, L. Wu, Y. Kong, Y. Zhang and J. Xu, *Chin. J. Lumin.*, 2022, **43**, 1361–1379.

17 X. Wang, P. Boutinaud, L. Li, J. Cao, P. Xiong, X. Li, H. Luo and M. Peng, *J. Mater. Chem. C*, 2018, **6**, 10367.

18 J. Cheng, P. Li, Z. Wang, Z. Li, M. Tian, C. Wang and Z. Yang, *Dalton Trans.*, 2018, **47**, 4293.

19 L. Li, K. Wong, P. Li and M. Peng, *J. Mater. Chem. C*, 2016, **4**, 8166.

20 H. Matsui, C. Xu, Y. Liu and H. Tateyama, *Phys. Rev. B: Condens. Matter Mater. Phys.*, 2004, **69**, 235109.

21 W. Chen, G. Li, J.-O. Malm, Y. Huang, R. Wallenberg, H. Han, Z. Wang and J.-O. Bovin, *J. Lumin.*, 2000, **91**, 139–145.

22 L. Zhang, K. Shi, Y. Wang, L. Su, G. Yang, B. Huang, J. Kong, X. Dong and Z. Wang, *Nano Energy*, 2021, **85**, 106005.

23 H. Wang, X. Chen, J. Li, M. Li, K. Liu, D. Yang, S. Peng, T. Zhao, B. Zhao, Y. Li, Y. Wang, C. Lin and W. Yang, *ACS Appl. Mater. Interfaces*, 2023, **15**, 28204–28214.

24 H. Chen, L. Wu, F. Bo, J. Jian, L. Wu, H. Zhang, L. Zheng, Y. Kong, Y. Zhang and J. Xu, *J. Mater. Chem. C*, 2019, **7**, 7096.

25 L. Wu, S. Sun, Y. Bai, Z. Xia, L. Wu, H. Chen, L. Zheng, H. Yi, T. Sun, Y. Kong, Y. Zhang and J. Xu, *Adv. Opt. Mater.*, 2021, **9**, 2100870.

26 D. Zhao, S. Zhu, R. Zhang, Q. Yao, W. Liu and Y. Xue, *Inorg. Chem.*, 2021, **60**, 17942–17951.

27 F. Jiang, S. Sha, S. Li, S. Xu, H. Xu, X. Mei and Y. Zhang, *Ceram. Interfaces*, 2021, **47**, 13776–13782.

28 L. Zeng, A. Huegel, E. Helgren, F. Hellman, C. Piamonteze and E. Arenholz, *Appl. Phys. Lett.*, 2008, **92**, 142503.

29 H. Hu, H.-C. He, R.-K. Xie, C. Cheng, T. Yan, C. Chen, D. Sun, T.-S. Chan, J. Wu and L. Zhang, *Nano Energy*, 2022, **99**, 10739.

30 H. Chen, Y. Bai, L. Zheng, L. Wu, L. Wu, Y. Kong, Y. Zhang and J. Xu, *J. Mater. Chem. C*, 2020, **8**, 6587.

31 C. Chen, Z. Lin, H. Huang, X. Pan, T.-L. Zhou, H. Luo, L. Jin, D. Peng, J. Xu, Y. Zhuang and R.-J. Xie, *Adv. Funct. Mater.*, 2023, **33**, 2304917.

32 J. Zhang, G. Cai, W. Wang, L. Ma, X. Wang and Z. Jin, *Inorg. Chem.*, 2019, **59**, 2241–2247.

33 S. Liu, S. Zhang, N. Mao, Z. Song and Q. Liu, *J. Am. Ceram. Soc.*, 2020, **103**, 6793–6800.

34 Z. Wang, Y. Xiao, B. Liu, K. Chen, P. Shao, Z. Chen, P. Xiong, J. Gan and D. Chen, *Adv. Opt. Mater.*, 2023, **12**, 2301796.

35 J. Kang, X. Yang, Q. Hu, Z. Cai, L. M. Liu and L. Guo, *Chem. Rev.*, 2023, **123**, 8859–8941.

36 P. Zhang, Z. Zheng, L. Wu, Y. Kong, Y. Zhang and J. Xu, *Inorg. Chem.*, 2021, **60**, 18432–18441.

37 Z. Zhou, S. Zhang, Y. Le, H. Ming, Y. Li, S. Ye, M. Peng, J. Qiu and G. Dong, *Adv. Opt. Mater.*, 2022, **10**, 2101669.

38 J. Wang, H. Zhang, B. Lei, H. Dong, H. Zhang, Y. Liu, M. Zheng, Y. Xiao and R. J. Xie, *J. Am. Ceram. Soc.*, 2015, **98**, 1823–1828.

39 W. Meng, P. Cai, X. Fu and H. Zhang, *J. Lumin.*, 2022, **248**, 11883.

40 P. Zhang, X. Chen, Y. Bai, X. Zhao, X. Fu, L. Wu, Y. Wang, T. Sun, Y. Kong, Y. Zhang and J. Xu, *Adv. Opt. Mater.*, 2023, **12**, 2301406.

41 Y. Tang, Y. Cai, K. Dou, J. Chang, W. Li, S. Wang, M. Sun, B. Huang, X. Liu, J. Qiu, L. Zhou, M. Wu and J. Zhang, *Nat. Commun.*, 2024, **15**, 3209.